Journal Pre-proof

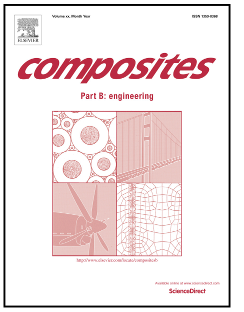

Micromechanical response of two-dimensional transition metal carbonitride (MXene) reinforced epoxy composites

Christine B. Hatter, Jay Shah, Babak Anasori, Yury Gogotsi

PII: S1359-8368(19)32569-7

DOI: https://doi.org/10.1016/j.compositesb.2019.107603

Reference: JCOMB 107603

To appear in: *Composites Part B*

Received Date: 20 June 2019

Revised Date: 27 August 2019

Accepted Date: 13 November 2019

Micromechanical Response of Two-Dimensional Transition Metal Carbonitride (MXene) Reinforced Epoxy Composites

Christine B. Hatter[1], Jay Shah[1], Babak Anasori[2], Yury Gogotsi[1*]

[1]A.J. Drexel Nanomaterials Institute and Department of Materials Science and Engineering, Drexel University, 3141 Chestnut St., Philadelphia, PA, 19104, USA

[2]Integrated Nanosystems Development Institute and Department of Mechanical and Energy Engineering, Indiana University-Purdue University Indianapolis, 723 W. Michigan St, Indianapolis, IN 46202, USA

Corresponding author: Gogotsi@drexel.edu

Abstract: MXenes have attracted much attention as fillers in polymer composites due to their superior electrical and mechanical properties making them ideal for creating multifunctional composites. In this work, Ti_3CN-epoxy composites were prepared via solvent processing and cured with amine-based hardener. The effects of Ti_3CN content in the epoxy system on the thermal degradation behavior and micromechanical properties were investigated. The extent of intercalation of epoxy into MXene flakes was analyzed by transmission electron microscopy. Nanoindentation analysis of MXene-epoxy composites exhibited improved mechanical properties with increasing MXene content with highest increase of 12.8 GPa Young's modulus for 90 wt% Ti_3CN. An increase in creep resistance of composites was observed at maximum loading of Ti_3CN by 46% compared to neat epoxy.

Keywords: MXene; polymer composites; multifunctional materials; MXene-epoxy; nanocomposites; nanoindentation; mechanical properties

1. Introduction

Epoxy resins are the most commonly used thermosetting polymers in composites for aerospace, coatings, hardware components, and adhesives [1]. Due to good adhesion properties and thermal stability coupled with sufficient chemical resistance, epoxies are ideal for composite matrix materials [2, 3]. However, success in each application is dependent on mechanical stability including high tensile strength, stiffness, and modulus. Addition of nanoscale fillers has been shown to be an effective technique for improving mechanical properties of epoxy as well as electrical conductivity and other properties producing multifunctional composites. The most common nanofillers used are carbon nanotubes [4-6], nanoclay [7, 8], and graphene. Early works such as Schadler *et al.* have shown CNTs at low loadings of 5 wt% and decent dispersion can improve both tensile and compression moduli from 3.1 to 3.71 GPa and 3.63 to 4.65 GPa, respectively [9, 10]. However, with the discovery of graphene, properties of epoxy composites could be improved further. A study by Yang *et al.* proved that introducing graphene in combination with CNTs at 1wt% loadings can improve modulus, tensile strength and thermal conductivity 27%, 35%, 146%, respectively, compared to neat epoxy [11].

As a single sheet of covalently bonded carbon atoms, graphene has been shown to be the strongest material to date with Young's modulus of 1 TPa and tensile strength up to 130 GPa for perfect monolayers justifying its use for reinforcing polymers and its two-dimensional (2D) nature provides a high surface area [1, 12, 13]. Rafiee *et al*. showed previously graphene platelet content at 0.1 wt% outperformed both single and multiwalled carbon nanotubes of the same content in both Young's modulus and tensile strength 3.74 GPa and 78 MPa, respectively [14]. Further studies on fracture toughness of graphene/epoxy composites with 0.125 wt% increased toughness by 65% followed by a decrease with increasing concentration up to 0.5 wt% [15]. The observed decrease can be directly related to graphene dispersion throughout the polymer matrix. For example, Tang *et al.* compared extent of graphene dispersion and revealed poorly dispersed filler resulted in a minor shift of Tg of the composites as well as limited or decreased mechanical properties compared to neat epoxy and highly dispersed samples [16]. Additionally, lack of surface terminations limits processability of pristine graphene in polymer composite systems, leading to aggregation and easy pull-out of graphene flakes. As a result, graphene oxide derivatives have been incorporated into epoxy systems, where oxygen terminated graphene sheets, provide a solution processible alternative to inert graphene. However, mechanical properties of graphene oxide are significantly decreased due to the presence of surface functionalities with Young's modulus for graphene oxide near ~ 200 GPa [3, 14, 17-21].

MXenes are a family of 2D transition metal carbides, nitrides, and carbonitrides with the formula of $M_{n+1}X_nT_x$, where M is an early transition metal (e.g., Ti, Mo, V), X is carbon and/or nitrogen, T_x are surface functional groups, and n = 1-3. The aqueous medium during MXene synthesis produces surface moieties (T_x) such as –O, –OH, and –F resulting in hydrophilic 2D sheets that can be easily dispersed in water and various organic solvents [22, 23]. Among all the solution processed 2D materials, $Ti_3C_2T_x$ MXenes have the highest metallic conductivity of about 10,000 S/cm for solution processed films and the highest Young's modulus of 330 ± 30 GPa for a single flake $Ti_3C_2T_x$ [24-26]. This combination of properties makes MXenes a good candidate as fillers in epoxy composites. Previous studies have shown that MXenes can be incorporated into various polymers such as polyvinyl alcohol, polypyrrole, and sodium alginate with improved electrochemical performances and electromagnetic interference shielding [27-30]. So far, about 30 different MXenes have already been reported [22, 31, 32]. However, very few studies have investigated mechanical properties of bulk epoxy composites with MXene fillers.

Zhang *et al.* reported MXene-epoxy composites using imidazoles for crosslinking the epoxy network and MXene powder. It was shown that incorporating a M_2X MXene (Ti_2C) improved creep resistance, glass transition temperature as well as viscoelastic properties of the composites at low MXene content, but overall thermal stability was reduced [33]. However, mechanical properties of M_2X MXenes are considerably weaker than M_3X_2 structures [34, 35].

Here we report synthesis of Ti_3CN, we omit the T_x from the formula for simplicity, MXene-epoxy composites using solvent processing and amine-based hardener system. Nanoindentation analysis was used to determine micromechanical properties and microhardness of the resultant composites. To our knowledge, this is the first study reporting mechanical properties via nanoindentation on M_3X_2 MXene-epoxy composites.

2. Experimental

2.1 Materials

Epoxy resin used was commercially available diglycidyl ether of bisphenol A (DGEBA) (Epon 828, Hexion). The amine curing agent was 4,4'-Methylenebis(cyclohexylamine) (PACM, Sigma Aldrich). Ti_3AlCN MAX phase was used as the precursor for MXene synthesis as explained elsewhere [36]. All materials used for the MXene etching process such as hydrofluoric acid (HF, 49.5 wt%) and tetrabutylammonium hydroxide (TBAOH, 40wt% solution in water, Sigma Aldrich) were purchased from Acros Organics.

2.2 Synthesis of Ti_3CN MXene

Ti_3CN MXene was prepared using previously documented HF etching method [36, 37]. One gram of Ti_3AlCN MAX phase powder (particle size < 44 µm) was added to 20 mL of 15%

HF aqueous solution and stirred for 18 h at 35°C. Resultant solution was combined with deionized (DI) water in 50 mL centrifuge tubes and centrifuged at 3500 rpm for 3-5 minutes. The supernatant was decanted and remaining sediment was redispersed in DI water and centrifuged again followed by decanting. This washing process was repeated 4-5 times until a pH > 5 was obtained. After the final centrifugation, the sediment was collected as multilayer Ti_3CN (ML-Ti_3CN) powder through vacuum assisted filtration (VAF).

2.3 Delamination of Ti_3CN MXene

To delaminate the multilayer powder, one gram of ML-Ti_3CN powder was combined with 10 mL of TBAOH solution and stirred at room temperature for 1-2 h [36]. ML-Ti_3CN-TBAOH solution was then washed using DI water and centrifuged at 3500 rpm for 2-5 minutes to remove excess TBAOH. DI water was added again to the remaining sediment and transferred to a 50 mL glass bottle. A probe sonicated was placed in the glass bottle while the glass bottle was kept in a cooling system with a set temperature at -10 °C and probe sonicated for 1 h at 50% amplitude. After sonication, solution was centrifuged at 3500 rpm for 1 h and dark supernatant was collected containing delaminated Ti_3CN (d-Ti_3CN). VAF was used to collect a film of d-Ti_3CN, which then stored under vacuum at room temperature for future experiments.

2.4 Preparation of epoxy/Ti_3CN composites

For preparing composites with different MXene-epoxy weight ratios, appropriate amounts of d-Ti_3CN were dispersed in 5-10 mL of acetone in 20-mL glass vials. Mixture was then bath sonicated (Ultrasonic bath 2.8L, Fisher Scientific) for 5-6 h to fully redisperse d-Ti_3CN into acetone. Epoxy resin and PACM were weighed and combined in a separate 20-mL glass vial and then Ti_3CN-acetone dispersion was added. The composite mixtures were placed in a speed mixer (ARE-250, Thinky) at 2000 rpm for 10 minutes followed by bath sonication for 5 minutes. Composite samples of various Ti_3CN concentrations were synthesized (5, 10, 20, 40, 50, 80, 90 wt% of Ti_3CN) using this process. Samples were left in fume hood at room temperature for 2-3 days to allow acetone to evaporate. After solvent removal, all composite samples were degassed under vacuum for 1 h followed by a 2-step curing process, first at 80 °C for 4 h followed by 160°C overnight (~15 h) in air. A schematic of the Ti_3CN-epoxy composite synthesis process is presented in Figure 1.

2.5 Characterization

Morphology and structure of pure Ti_3CN and microtomed samples of Ti_3CN-epoxy composites were investigated using transmission electron microscopy (TEM, JEOL-2100, Japan) at 200 kV acceleration voltage. X-ray diffraction (XRD) was carried out using a Rigaku Smartlab (Tokyo, Japan) diffractometer with Cu-Kα radiation (40 kV and 44 mA) with step scan 0.04°, 3°-70° 2 theta range, step time of 0.5 s, 10 x 10 mm^2 window slit. Surface analysis of Ti_3CN-epoxy composites were investigated by scanning electron microscopy (SEM, Zeiss Supra 50VP, Germany). Composite samples were mounted in commercial resin and cured followed by ultramicrotomy for cross-section analysis in TEM. Additionally, aqueous solution of pure Ti_3CN flakes was also prepared and dropcast onto lacey carbon TEM copper grids. Thermal degradation properties were measured in Ar using thermal gravimetric analysis (TGA, SDT Q650, Discovery Series) using a ramp heating rate of 10 °C/min from room temperature to 1000 °C.

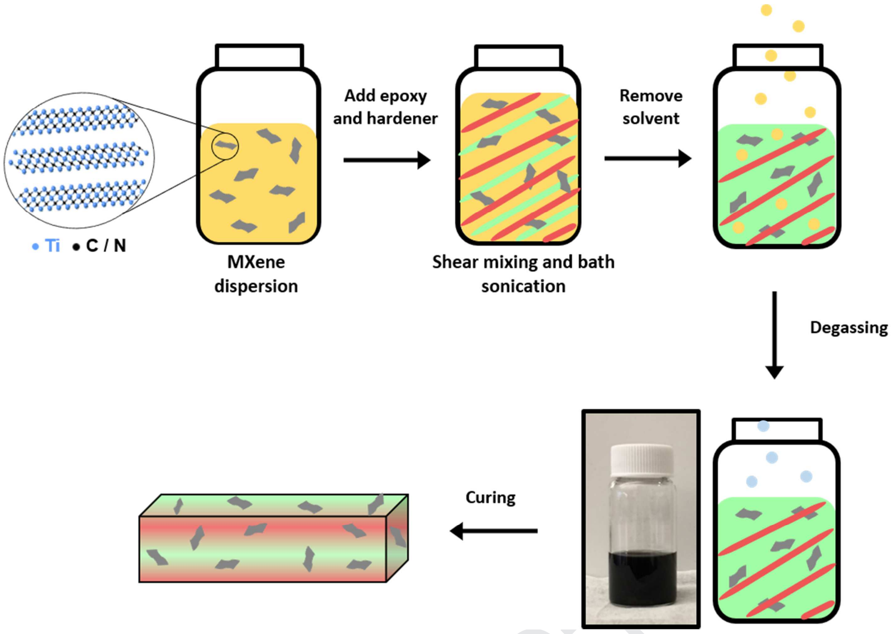

Figure 1. Schematic of synthesis process for solution processed Ti_3CN-epoxy composites. Acetone dispersions of delaminated Ti_3CN MXene were prepared using probe sonication then added to epoxy-hardener mix followed by high-speed mixing and additional bath sonication. Solvent (acetone) was evaporated from mixture at room temperature followed by degassing and two-step curing process.

Micromechanical properties were measured via nanoindentation measurements using Nano Indenter XP (MTS, USA). Prior to nanoindentation, Ti_3CN-epoxy composites were mounted in commercial epoxy-hardener system and allowed to cure overnight. Sample surfaces were then polished by sandpapers starting with course grit to fine grit of 400, 600, 800, and 1200 followed by polishing with diamond suspensions of 3, 1 and 0.5 µm using appropriate polishing cloth and diamond suspension. Spherical diamond indenter tip with 5 µm radius was used and calibrated on fused silica at room temperature. For each sample, 15 to 20 indents were made at various locations on the polished sample surface to ensure a statistically reliable account of material response. As a comparison, pure as-produced d-Ti_3CN film and neat epoxy samples were also mounted in commercial epoxy and prepared for nanoindentation. Vickers microhardness measurements, at various loads from 50 to 500 gF, were also performed for macroscale analysis of Ti_3CN-epoxy composites.

3. Results and Discussion

3.1 Characterization of Ti_3CN

Morphology of single-layer Ti_3CN flakes was studied using TEM as shown in Figure 2a. Average flake size varied in lateral dimensions from 500 nm up to 1 µm while thickness was about 1 nm after etching. The smaller lateral size of the flakes is due to the sonication process which causes MXene flakes to break from initial few-micrometer size reducing their dimensions, however this is strongly dependent on sonication time and power as shown with $Ti_3C_2T_x$ MXene [38]. Furthermore, Ti_3CNT_x demonstrates similar surface functional groups such as -O, -OH, and -F as other MXenes due to the HF etching process. Electronic properties, however, are also etching dependent and can vary from 270 mS/cm to 1100 S/cm [24, 37, 39]. XRD also confirmed lattice spacing of resultant MXene. In Figure 2b, the typical XRD pattern of VAF d-Ti_3CN is shown (bottom pattern) where its (002) peak position is at ~ 4.8º, which correspond to an interlayer spacing of 18.4 Å. This large interlayer spacing in the pristine d-Ti_3CN corresponds to the size of the TBA^+ cation intercalated MXene layers [24]. Additionally, only the 00*l* reflection are present in the d-Ti_3CN which confirms the complete delamination of the Ti_3CN powder.

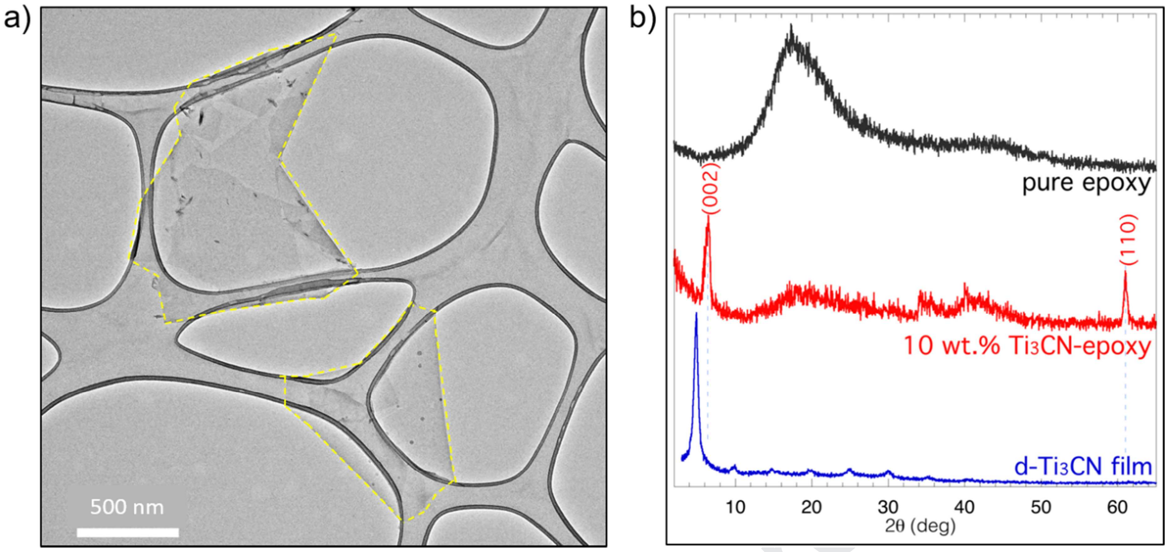

Figure 2. TEM image of as-produced single flakes of Ti_3CN MXene (a), and x-ray diffraction patterns for pure d-Ti_3CN film, 10 wt% Ti_3CN-epoxy, and neat epoxy samples.

3.2 Structural characterization of Ti_3CN-epoxy nanocomposites

XRD patterns for pure Ti_3CN film, 10 wt% Ti_3CN-epoxy composite, and neat epoxy are presented in Figure 2b. The neat epoxy and 10 wt% Ti_3CN-epoxy composite patterns show the characteristic broad epoxy peak from 14° to 24° due to the scattering of cured epoxy molecules [40, 41]. In addition, the (*002*) MXene peak is shifted to higher 2θ of ~ 6.3° corresponding to a decrease in interlayer spacing to ~14 Å. This shift indicates that the TBA^+ cations have been removed from MXene interlayer spacing and might be replaced by epoxy [24]. However, unlike the pure d-Ti_3CN XRD pattern (Figure 2b, bottom pattern) that only the (*00l*) reflections appear, different Ti_3CN reflections appear in the composite samples, including the peaks from ~30° to 45° and the 110 peak at ~ 61°. It has been shown previously that the appearance or disappearance of certain MXene reflections in XRD patterns is due to the preferred orientation of the MXene flakes in the VAF films as well as the orientation of the film with respect to the x-ray beam. For example, when a VAF MXene film is placed flat on the XRD machine sample holder (horizontal orientation), only the (*00l*) peaks present, similar to pure d-Ti_3CN film pattern here. However, when MXene film was rotated by 90º, the (*hk0*) peaks appear [42]. Presence of all the Ti_3CN reflections in the composite samples shows MXene flakes do not follow any preferred orientation and are stacked randomly in the epoxy matrix.

SEM images of the composite surfaces in Figure 3a indicate epoxy coated MXene sheets protruding from the sample surface for 50 wt% Ti_3CN (indicated by yellow arrows). Since MXene single flakes are approximately 1 nm thick with an average lateral size of 0.5 to 1 µm (Figure 2a), it is reasonable to conclude that the visible Ti_3CN particles in SEM are multiple layer stacks of MXene. These particles are different from multilayer particles observed after etching. In the latter, the multilayer particles keep the morphology of their MAX phase precursor Ti_3AlCN. However, since d-Ti_3CN was used for the composites, all large multilayer particles from etching were removed before collecting delaminated MXene via VAF. The Ti_3CN particles seen in SEM show that the restacked MXene single flakes during VAF were not fully redispersed or might have restacked in epoxy during the fabrication process. To assess the dispersion of Ti_3CN flakes within the epoxy network, cross-sections of composite samples were prepared and analyzed using TEM. High-resolution images in Figure 3b show mostly isotropic dispersion of Ti_3CN fillers throughout composite post-curing. Spacing between MXene sheets varied from 17 – 23 Å indicating epoxy was intercalated between Ti_3CN sheets, causing a random spacing between MXene sheets which most likely decreases presence of strong reflections in XRD. However, some aggregates were observed within the polymer matrix, most likely due to the original d-Ti_3CN film not fully redispersed into the acetone solution, those which gave the reflection in the XRD pattern of the composite in Figure 2b. For the first time, bent MXene flakes were observed throughout the Ti_3CN-epoxy composites. MXenes typically have a higher bending rigidity compared to graphene and only planar flakes were observed in polyvinyl alcohol, sodium alginate, and other matrices [27-29, 43].

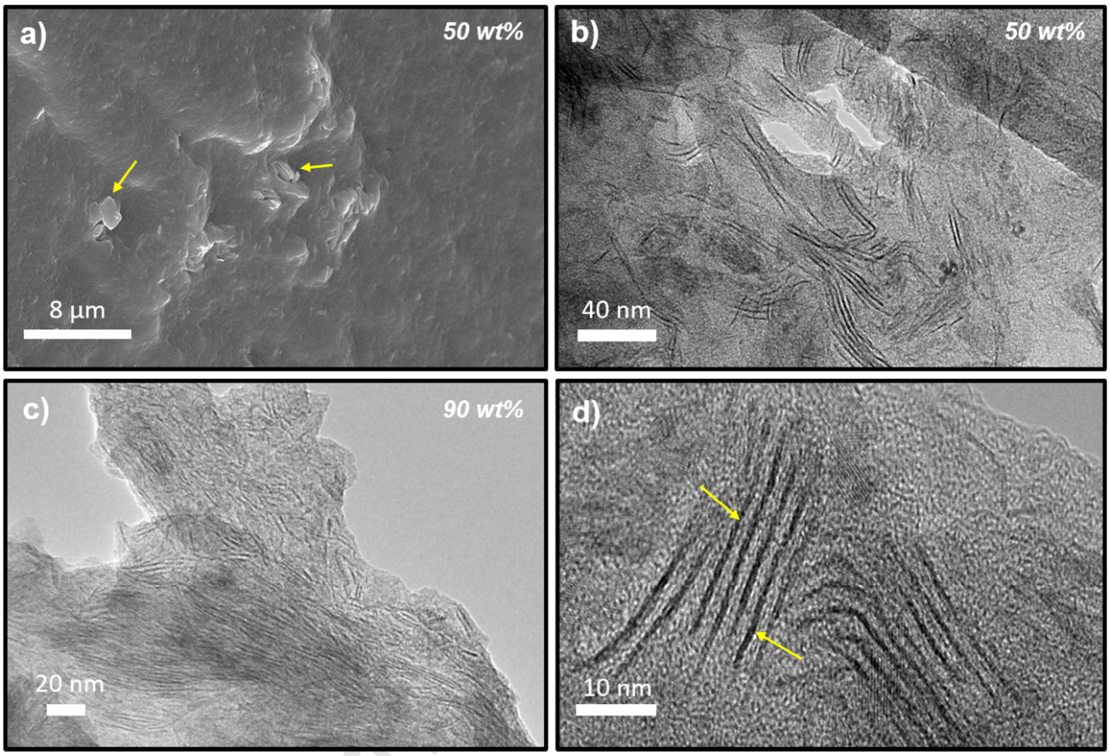

Figure 3. Microscopic analysis of 50 wt% and 90 wt% Ti_3CN-epoxy composites. Secondary electron SEM images of restacked multilayer Ti_3CN protruding from the sample surface coated in epoxy (a). Cross-section TEM images of composites (b-d) indicating good dispersion of Ti_3CN within epoxy matrix and intercalation of epoxy molecules between MXene flakes (dark lines) (d).

3.3 Thermal stability of Ti_3CN-epoxy nanocomposites

Nanomaterials incorporated as fillers are traditionally used to improve overall mechanical properties of epoxy, however, they can also be used for expanding the operating temperature window of the resulting composite [44]. TGA measurements were performed on Ti_3CN-epoxy composites to assess their thermal stability. Figure 4a shows individual thermogravimetric curves for composites with varying MXene content. For neat epoxy cured using PACM, degradation occurs around 370 °C. A slight improvement was observed at 5 wt% loading of Ti_3CN, slowing the onset of degradation to approximately 380 °C. Ti_3CN-epoxy composites with MXene content higher than 5 wt% showed a decrease in degradation temperature as seen in Figure 4b. This decrease in degradation temperature at higher MXene contents is influenced by the Ti_3CN dispersion throughout the matrix. In the presence of fillers, polymer chains experience restricted movement and require increased temperatures for molecular chain motion [45, 46]. Negatively

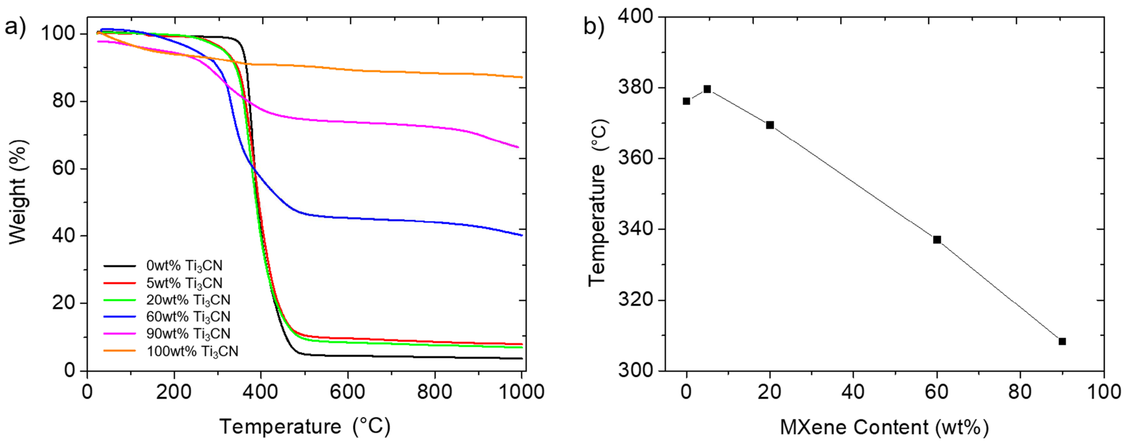

charged MXene flakes can also adsorb amine-based hardener molecules and effect the resulting epoxy structure after curing.

Figure 4. Thermogravimetric curves of MXene-epoxy composites with varying Ti_3CN content (a) and comparison of degradation temperatures showing a decrease in onset of degradation with increasing MXene content (b). Line connecting points in (b) is a guide for the eye.

3.4 Mechanical properties of Ti_3CN-epoxy nanocomposites

Nanoindentation measurements at room temperature were used to determine micromechanical response of Ti_3CN – epoxy composites of varying MXene content. Previous studies have utilized Berkovich indenters, however much information for the elastic and elastic-to-plastic deformation region is lost due to immediate plastic deformation during indentation [47-

50]. Here, a spherical indenter of 5μm radius was used to capture elastic properties of the composites. Young's modulus was extracted following previously studied Oliver and Pharr method [51]. The spherical indentation model is based on the Hertz theory in the elastic region [51-53]

$$P = \frac{4}{3} E_{\text{eff}} R_{\text{eff}}^{1/2} h_{\text{e}}^{3/2} \tag{1}$$

$$a = \sqrt{R_{\text{eff}} h_{\text{e}}} \tag{2}$$

where a is the contact radius at the indentation load P, and h_e is the elastic penetration depth. R_{eff} is the effective radius and E_{eff} denotes effective Young's modulus of the indenter and the specimen system. This can be further simplified to the following expression

$$\frac{\mathrm{P}}{\pi a^2} = \frac{4}{3\pi} \mathrm{E}_{\text{eff}} \left(\frac{a}{\mathrm{R}}\right) \tag{3}$$

where the left side of the equation represents the indentation stress and the expression in parentheses on the right side represents the indentation strain [47]. Applying this model allows for an estimation of Young's modulus. In the Oliver and Pharr method, Eq. 1 is recast as

$$E_{\text{eff}} = \frac{S}{2a} \tag{4}$$

where S (= dP/dh_e) is the sample stiffness for indentations using spherical indenters.

Figure 5a displays typical load-displacement curves obtained from Ti_3CN-epoxy samples. It has been shown that M_3X_2 MXene (Ti_3C_2) has the highest Young's modulus for solution-processed two-dimensional materials [25]. Due to the nature of MXene, the presence of flakes improves rigidity of the composite. Pure Ti_3CN had the highest mechanical properties measured by indentation while neat epoxy required the lowest load at 53 mN and 14 mN, respectively, to reach a set displacement of 2 μm. Mechanical property improved in all the composite samples with increasing Ti_3CN content. Additionally, samples were indented at a constant loading of 20 mN over a 10 s time interval to assess resistance to mechanical deformation under load (creep) (Figure 5b). Measurements revealed a 37% decrease in creep when Ti_3CN content was increased to 40 wt% compared to neat epoxy. This was further improved to 46% when MXene content reached 90 wt%, with pure Ti_3CN showing the smallest displacement at constant loading.

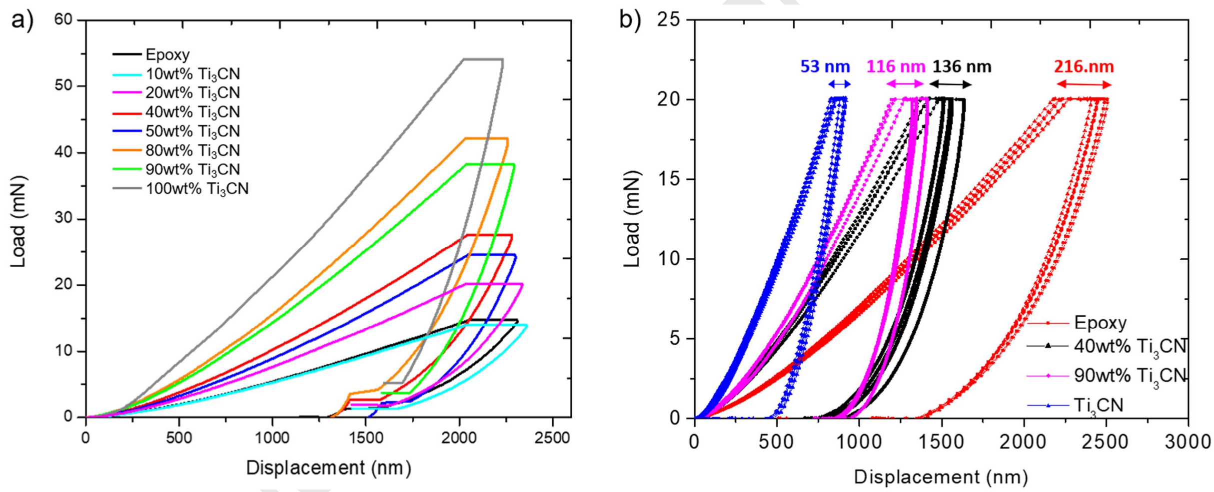

Improvement in mechanical stability of the Ti_3CN-epoxy samples is likely due to good dispersion of MXene throughout the epoxy matrix and efficient stress transfer at the MXene-epoxy interface.

Figure 5. Load-displacement curves for neat epoxy, pure Ti_3CN, and Ti_3CN-epoxy composites of varying Ti_3CN content from 0 to100 wt% (a) and load-displacement curves at varying MXene content for studying creep resistance under constant load (b).

For determining Young's modulus of composite samples, E_{eff} can be found from the slope of the *S*-*a* curves (Figure 6a). To ensure the correct E_{eff} is calculated, zero-point correction factor developed by Moseson *et al.* was used [54]. Contact stiffness (*S*) information is obtained during nanoindentation measurements while contact radius (a) values are estimated using the following expression

$$a = \sqrt{2R_t h_c - h_c^2} \quad (5)$$

where h_c is the contact depth and R_t is the indenter tip radius. Zero-point correction provides an accurate and reliable determination of the 'zero point' where the indenter tip makes first contact with the sample surface, where both indentation load (P) and indentation depth would be zero [54, 55]. Figure 6a shows S-a plots for composites with varying content of Ti_3CN. As MXene concentration increase, the steepness of the S-a curves increased, resulting in larger calculated modulus values. Similar to maximum mechanical load behavior, pure Ti_3CN showed the highest Young's modulus nearly 3 times that of neat epoxy with 15 GPa and 4.5 GPa, respectively. The calculated modulus values and Vickers hardness measurements are shown in Figure 6b. When Ti_3CN filler concentration is increased to 40 wt%, the resulting composite shows a 93% increase in Young's modulus and 104% increase in microhardness compared to neat epoxy. Prior nanoindentation study by Gu *et al.* showed small changes (~6% improvement) in Young's modulus with addition of graphene nanoplatelets up to 25 wt% compared to neat epoxy indicating limited transfer of filler properties to polymer matrix [56]. Another study observed a ~25% improvement in epoxy modulus when 6 wt% graphene content was added [57]. Furthermore, this improvement is significantly lower than the modulus improvement by Ti_3CN MXene in this study (Figure 6b). A maximum composite modulus of 12.8 GPa was reached at 90 wt% MXene corresponding to a 182% increase. The improvement in microhardness follows a similar trend and is in agreement with nanoindentation measurements. Extent of dispersion of Ti_3CN filler, in addition to good adhesion at the MXene-epoxy interface, allow effective stress transfer from the epoxy matrix for improved micromechanical response.

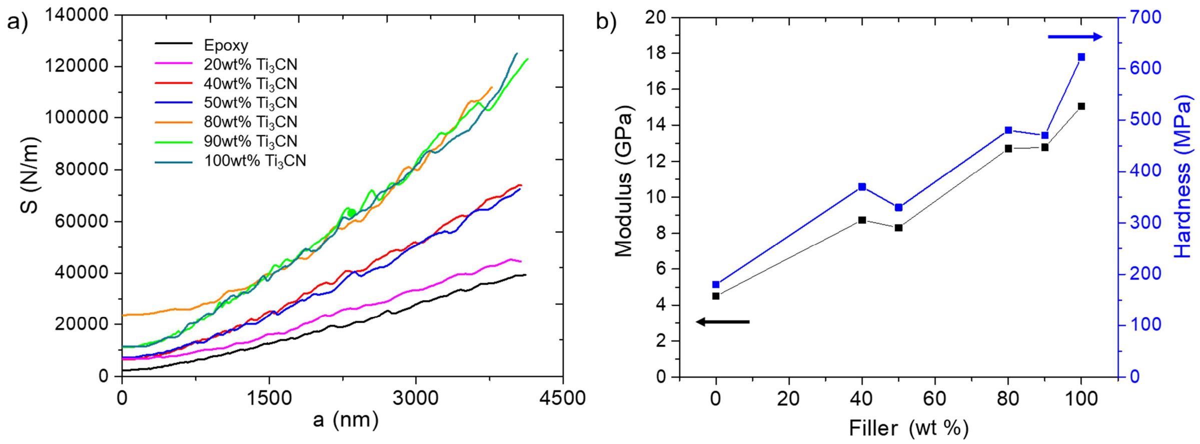

Figure 6. Plot of contact stiffness versus contact radius as determined from spherical nanoindentation with zero-point correction for composites with varying Ti_3CN content (a) and comparison of calculated Young's modulus and Vickers hardness values (b). Line connecting points is a guide for the eye.

4. Conclusion

We successfully fabricated the first transition metal carbonitride (Ti_3CN) MXene-epoxy composites through solvent processing. Micromechanical properties were assessed via spherical nanoindentation and Vickers indentation. TEM analysis revealed intercalation of epoxy between Ti_3CN sheets throughout the matrix, resulting in good dispersion and limited aggregation. Ti_3CN-epoxy composites showed improved mechanical performance as MXene content increased to 90 wt%, reaching the largest modulus improvement of 12.8 GPa about triple compared to neat epoxy. Nanoindentation also revealed improved creep resistance at constant load for composites with higher Ti_3CN content. Composite sample at 90 wt% Ti_3CN exhibited reduction in creep by 46% compared to neat epoxy. However, thermal stability of the nanocomposites with increasing Ti_3CN content exhibited a decrease. The MXene-epoxy interface plays an important role in optimization of mechanical properties of epoxy nanocomposites. Overall, the presence of Ti_3CN MXene fillers in epoxy displays clear improvement of mechanical properties over neat epoxy.

Acknowledgements
The authors thank Dr. Giuseppe Palmese and Dr. Santosh Yadav for their helpful discussions and use of laboratory equipment. This research is supported by the National Science Foundation under Grant No. 1740795. Any opinion, findings and conclusion or recommendations expressed in this material are those of the author(s) and do not necessarily reflect the reviews of the National Science Foundation. SEM and TEM analyses were performed at the Centralized Research Facilities (CRF) at Drexel University.

References

1. Domun N, Hadavinia H, Zhang T, Sainsbury T, Liaghat GH, Vahid S. Improving the fracture toughness and the strength of epoxy using nanomaterials–a review of the current status. Nanoscale, 2015; **7**(23): 10294-10329.
2. Liu S, Chevali VS, Xu Z, Hui D, Wang H. A review of extending performance of epoxy resins using carbon nanomaterials. Composites Part B: Engineering, 2018; 136: 197-214.
3. Wang F, Drzal LT, Qin Y, Huang Z. Mechanical properties and thermal conductivity of graphene nanoplatelet/epoxy composites. Journal of Materials Science, 2015; **50**(3): 1082-1093.
4. Spitalsky Z, Tasis D, Pagagelis K, Galiotis C. Carbon nanotube–polymer composites: chemistry, processing, mechanical and electrical properties. Progress in Polymer Science, 2010; **35**(3): 357-401.
5. Gojny F, Wichmann MHG, Kopke U, Fiedler B, Schukte K. Carbon nanotube-reinforced epoxy-composites: enhanced stiffness and fracture toughness at low nanotube content. Composites science and technology, 2004; **64**(15): 2363-2371.
6. Guo P, Chen X, Gao X, Song H, Shen H. Fabrication and mechanical properties of well-dispersed multiwalled carbon nanotubes/epoxy composites. Composites Science and Technology, 2007; **67**(15-16): 3331-3337.
7. Jin F-L, X. Li, Park SJ. Synthesis and application of epoxy resins: A review. Journal of Industrial and Engineering Chemistry, 2015; **29**: 1-11.
8. Zabihi O, Ahmadi M, Nikafshar S, Preyeswary KC, Naebe M. A technical review on epoxy-clay nanocomposites: Structure, properties, and their applications in fiber reinforced composites. Composites Part B: Engineering, 2017; 135:1-24.
9. Schadler L S, Giannaris S C, Ajayan P M, Load transfer in carbon nanotube epoxy composites. Applied Physics Letters, 1998; **73**(26): 3842-3844.
10. Thostenson E T, Ren Z, Chou T W, Advances in the science and technology of carbon nanotubes and their composites: a review. Composites Science and Technology, 2001; **61**(13): 1899-1912.
11. Yang S Y, Lin W-N, Huang Y-L, Tien H-W, Wang J-Y, Ma C-C M, Li S-M, Wang Y-S, Synergetic effects of graphene platelets and carbon nanotubes on the mechanical and thermal properties of epoxy composites. Carbon, 2011; **49**(3): 793-803.

12. Novoselov KS, Geim AK, Morozov SV, Jiang D, Zhang Y, Dubonos SV, Grigorieva IV, Firsov AA. Electric field effect in atomically thin carbon films. Science, 2004; **306**(5696): 666-669.
13. Zaman I, Manshoor B, Khalid A, Araby S, From clay to graphene for polymer nanocomposites—a survey. Journal of Polymer Research, 2014; **21**(5): 429.
14. Rafiee M A, Rafiee J, Wang Z, Song H, Yu Z-Z, Koratkar N, Enhanced mechanical properties of nanocomposites at low graphene content. ACS nano, 2009; **3**(12): 3884-3890.
15. Rafiee M A, Rafiee J, Srivastava I, Wang Z, Song H, Yu Z-Z, Koratkar N, Fracture and fatigue in graphene nanocomposites. Small, 2010; **6**(2):c179-183.
16. Tang L-C, Wan Y-J, Yan D, Pei Y-B, Zhao L, Li Y-B, Wu L-B, Jiang J-X, Lai G-Q, The effect of graphene dispersion on the mechanical properties of graphene/epoxy composites. Carbon, 2013; **60**: 16-27.
17. Singh V, Joung D, Zhai L, Das S, Khondaker SI, Seal S. Graphene based materials: past, present and future. Progress in materials science, 2011; **56**(8): 1178-1271.
18. Suk JW, Piner RD, An J, Ruoff RS. Mechanical properties of monolayer graphene oxide. ACS Nano, 2010; **4**(11): 6557-6564.
19. Ribeiro H, Silva W M, Neves J C, Calado H D, Paniago R, Seara L M, Camarano D M, Silva G G, Multifunctional nanocomposites based on tetraethylenepentamine-modified graphene oxide/epoxy. Polymer Testing, 2015; **43**: 182-192.
20. Tung T T, Karunagaran R, Tran D N H, Gao B, Nag-Chowdhury S, Pillin I, Castro M, Feller J-F, Losic D, Engineering of graphene/epoxy nanocomposites with improved distribution of graphene nanosheets for advanced piezo-resistive mechanical sensing. Journal of Materials Chemistry C, 2016; **4**(16): 3422-3430.
21. Klimek□McDonald D R, King J A, Miskioglu I, Pineda E J, Odegard G M, Determination and modeling of mechanical properties for graphene nanoplatelet/epoxy composites. Polymer Composites, 2018; **39**(6): 1845-1851.
22. Anasori B, Lukatskaya MR, Gogotsi Y. 2D metal carbides and nitrides (MXenes) for energy storage. Nature Reviews Materials, 2017; **2**(2): 16098.
23. Maleski K, Mochalin V N, Gogotsi Y. Dispersions of Two-Dimensional Titanium Carbide MXene in Organic Solvents. Chemistry of Materials, 2017; **29**(4): p. 1632-1640.
24. Hantanasirisakul K, Alhabeb M, Lipatov A, Maleski K, Anasori B, Salles P, Ieosakulrat C, Pakawatpanurut P, Sinitskii A, May S J, Gogotsi Y. Effects of Synthesis and Processing on Optoelectronic Properties of Titanium Carbonitride MXene. Chemistry of Materials, 2019.
25. Lipatov A, Lu H, Alhabeb M, Anasori B, Gruverman A, Gogotsi Y. and Sinitskii A. Elastic Properties of 2D Ti3C2Tx MXene Monolayers and Bilayers. Science, 2018.
26. Sarycheva A, Polemi A, Liu Y, Dandekar K, Anasori B, Gogotsi, Y. 2D titanium carbide (MXene) for wireless communication. Science Advances, 2018; **4**(9).
27. Ling Z, Ren CE, Zhao MQ, Yang J, Giammarco JM, Qiu J, Barsoum MW, Gogotsi Y. Flexible and conductive MXene films and nanocomposites with high capacitance. Proceedings of the National Academy of Sciences, 2014; **111**(47): 16676-16681.
28. Boota M, Anasori B, Voigt C, Zhao MQ, Barsoum MW, Gogotsi Y. Pseudocapacitive Electrodes Produced by Oxidant□Free Polymerization of Pyrrole between the Layers of 2D Titanium Carbide (MXene). Advanced Materials, 2016; **28**(7): 1517-1522.
29. Shahzad F, Alhabeb M, Hatter CB, Anasori B, Hong SM, Koo CM, Gogotsi Y. Electromagnetic interference shielding with 2D transition metal carbides (MXenes). Science, 2016. **353**(6304): p. 1137-1140.
30. Mirkhani SA, Shayesteh Zeraati A, Aliabadian E, Naguib M, Sundararaj U. High Dielectric Constant and Low Dielectric Loss via Poly (vinyl alcohol)/Ti3C2Tx MXene Nanocomposite. ACS Applied Materials & Interfaces, 2019.
31. Verger L, Xu C, Natu V, Cheng HM, Ren W, Barsoum MW. Overview of the synthesis of MXenes and other ultrathin 2D transition metal carbides and nitrides. Current Opinion in Solid State and Materials Science, 2019.

32. Anasori B, Gogotsi Y. 2D Metal Carbides and Nitrides (MXenes): Structure, Properties and Applications. Springer International Publishing 2019.
33. Zhang H, Wang L, Zhou A, Shen C, Dai Y, Liu F, Chen J, Li P, Hu Q. Effects of 2-D transition metal carbide Ti 2 CT x on properties of epoxy composites. RSC Advances, 2016; **6**(90): 87341-87352.
34. Plummer G, Anasori B, Gogotsi Y, Tucker GJ. Nanoindentation of monolayer Tin+ 1CnTx MXenes via atomistic simulations: The role of composition and defects on strength. Computational Materials Science, 2019; **157**: 168-174.
35. Kurtoglu M, Naguib M, Gogotsi Y, Barsoum MW. First principles study of two-dimensional early transition metal carbides. MRS Communications, 2012; **2**(4): 133-137.
36. Naguib M, Unocic RR, Armstrong BL, Nanda J. Large-scale delamination of multi-layers transition metal carbides and carbonitrides “MXenes”. Dalton Transactions, 2015; **44**(20): 9353-9358.
37. Naguib M, Mashtalir O, Carle J, Presser V, Lu J, Hultman L, Gogotsi Y, Barsoum MW. Two-dimensional transition metal carbides. ACS Nano, 2012; **6**(2): 1322-1331.
38. Maleski K, Ren CE, Zhao MQ, Anasori, B, Gogotsi Y. Size-dependent physical and electrochemical properties of two-dimensional MXene flakes. ACS Applied Materials & Interfaces, 2018; **10**(29): 24491-24498.
39. Hantanasirisakul K, Gogotsi Y, Electronic and optical properties of 2D transition metal carbides and nitrides (MXenes). Advanced Materials, 2018; **30** (52): 1804779.
40. Ma J, Meng Q, Michelmore A, Kawashima N, Izzuddin Z, Bengtsson C, Kuan HC. Covalently bonded interfaces for polymer/graphene composites. Journal of Materials Chemistry A, 2013; **1**(13): 4255-4264.
41. Wan YJ, Tang LC, Gong LX, Yan D, Li YB, Wu LB, Jiang JX, Lai GQ, Grafting of epoxy chains onto graphene oxide for epoxy composites with improved mechanical and thermal properties. Carbon, 2014; **69**: 467-480.
42. Ghidiu M, Barsoum MW. The {110} reflection in X□ray diffraction of MX ene films: Misinterpretation and measurement via non□standard orientation. Journal of the American Ceramic Society, 2017; **100**(12): 5395-5399.
43. Borysiuk VN, Mochalin VN, Gogotsi Y. Bending rigidity of two-dimensional titanium carbide (MXene) nanoribbons: A molecular dynamics study. Computational Materials Science, 2018; **143**: 418-424.
44. Ribeiro H, Silva WM, Rodrigues MTF, Neves JC, Paniago R, Fantini C, Calado HD, Seara LM, Silva GG. Glass transition improvement in epoxy/graphene composites. Journal of Materials Science, 2013; **48**(22): 7883-7892.
45. Monti M, Rallini M, Puglia D, Peponi L, Torre L, Kenny JM. Morphology and electrical properties of graphene–epoxy nanocomposites obtained by different solvent assisted processing methods. Composites Part A: Applied Science and Manufacturing, 2013; **46**: 166-172.
46. Yasmin A, Daniel IM. Mechanical and thermal properties of graphite platelet/epoxy composites. Polymer, 2004; **45**(24): 8211-8219.
47. Su C, Herbert EG, Sohn S, LaManna JA, Oliver WC, Pharr GM. Measurement of power-law creep parameters by instrumented indentation methods. Journal of the Mechanics and Physics of Solids, 2013; **61**(2): 517-536.
48. Fischer-Cripps AC. Critical review of analysis and interpretation of nanoindentation test data. Surface and coatings technology, 2006; **200**(14-15): 4153-4165.
49. Schwarzer N, Pharr GM. On the evaluation of stresses during nanoindentation with sharp indenters. Thin Solid Films, 2004; **469**: 194-200.
50. Bei H, George EP, Hay JL, Pharr GM. Influence of indenter tip geometry on elastic deformation during nanoindentation. Physical review letters, 2005; **95**(4): 045501.

51. Oliver WC, Pharr GM, Measurement of hardness and elastic modulus by instrumented indentation: Advances in understanding and refinements to methodology. Journal of Materials Research, 2004; **19**(1): 3-20.
52. Basu S, Moseson A, Barsoum MW. On the determination of spherical nanoindentation stress–strain curves. Journal of Materials Research, 2006; **21**(10): 2628-2637.
53. Buchs R, Basu S, Elshrief OA, Coward R, Barsoum MW, Spherical nanoindentation and Vickers microhardness study of the deformation of poled $BaTiO_3$ single crystals. Journal of Applied Physics, 2009; **105**(9): 093540.
54. Moseson AJ, Basu S, Barsoum MW. Determination of the effective zero point of contact for spherical nanoindentation. Journal of Materials Research, 2008; **23**(1): 204-209.
55. Kalidindi SR, Pathak S. Determination of the effective zero-point and the extraction of spherical nanoindentation stress–strain curves. Acta Materialia, 2008; **56**(14): 3523-3532.
56. Gu J, Liang C, Zhao X, Gan B, Qui H, Guo Y, Yang X, Zhang Q, Wang D-Y, *H*ighly thermally conductive flame-retardant epoxy nanocomposites with reduced ignitability and excellent electrical conductivities. Composites Science and Technology, 2017; **139**: 83-89.
57. King J A, Klimek D, Miskioglu I, Odegard G, Mechanical properties of graphene nanoplatelet/epoxy composites. Journal of Applied Polymer Science, 2013; **128**(6): 4217-4223.